analytical chemistry

Article

pubs.acs.org/ac

Signal-Amplified Near-Infrared Ratiometric Electrochemiluminescence Aptasensor Based on Multiple Quenching and Enhancement Effect of Graphene/Gold Nanorods/G-Quadruplex

Kang Shao,[†] Biru Wang,[†] Shiyi Ye,[†] Yunpeng Zuo,[†] Long Wu,[†] Qin Li,[†] Zhicheng Lu,[†] XueCai Tan,[‡] and Heyou Han*[,†]

[†]State Key Laboratory of Agricultural Microbiology, College of Science, College of Food Science and Technology, Huazhong Agricultural University, Wuhan 430070, People's Republic of China

[‡]School of Chemistry and Chemical Engineering, Guangxi University for Nationalities, Nanning 530008, People's Republic of China

Supporting Information

ABSTRACT: Dual-signaling ratiometric electrochemiluminescence (ECL) technology has attracted particular attention in analytical science due to its precise measurement to normalize variation in environmental changes. Creating new mated ECL report units with two emitting states and improving the detection sensitivity are major challenges for ratiometric ECL measurement. Here, we fabricate an ultrasensitive near-infrared ratiometric ECL aptasensor based on a dual-potential signal amplification strategy triggered by the quencher/enhancer [graphene/hemin/gold nanorods/G-quadruplex–hemin (rGO–H–AuNRs–G_4H) composite]. The composite was initially prepared through three consecutive steps: the π–π stacking interaction between hemin and graphene, in-site growth of AuNRs, and surface ligand exchange. Dual ECL quenching of quantum dots (QDs) and multiple signal enhancement of luminol can be achieved simultaneously by the fabrication of the sandwich "thrombin aptamer I (TBA_1)–TB–TBA_2 (rGO–H–AuNRs–G_4H)" mode: (i) the formation of three-dimensional G-quadruplex between aptamer and thrombin not only shortens the distance between the donor (QDs) and receptor (rGO–H and AuNRs) to trigger electrochemiluminescence energy transfer but also provides the place for intercalating hemin; (ii) the hemin intercalated into G_4 structure and hemin connected onto rGO together with AuNRs/rGO nanomaterials can achieve the multiple peroxidase-like catalysis of H_2O_2 to greatly enhance the ECL of luminol. The ratiometric ECL aptasensor self-calibrated by the internal reference (luminol or QDs) exhibits ultrasensitive and accurate analytical performance toward thrombin (TB) with a linear detection range from 100 ng/mL to 0.5 pg/mL and a detection limit of 4.2 fg/mL [defined as signal-to-noise ratio (S/N) = 3].

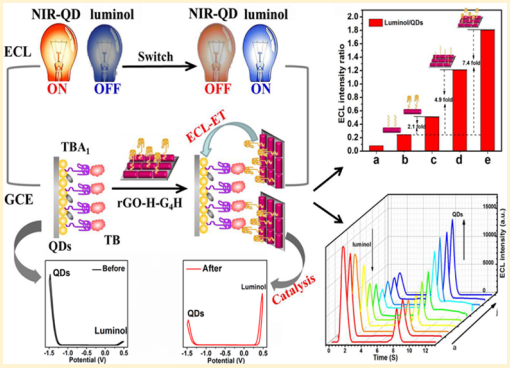

The sensitivity and accuracy of analytical methods play important roles in early detection of low-abundance and complex samples. Although a variety of signal amplification strategies of electrochemiluminescence (ECL) have been reported based on direct intermediates (electric conductor,[1−4] carrier,[5] magnetic bead,[6] catalyst,[7,8] bridge,[9] DNA,[10] organics,[11] etc.) or some modes (steric hindrance, resonance energy transfer, and so on), how to ensure the accuracy of the analytical method is also a major issue to be addressed. Compared to single-signal ECL measurement, ratiometric ECL strategy can provide more precise results under variable external environment and eliminate most ambiguous interference by the self-calibration of two emission bands.[12,13] Currently, creating new dual-emission ECL report units with potential-dependent properties is the major challenge to carry out ratiometric ECL measurements.[14] To address this challenge, a number of novel ECL ratiometric sensors have been developed.[15−17] Unfortunately, current ratiometric ECL sensing approaches are mainly confined to the visible region, which are always interfered by the tissue autofluorescence. In addition, most of clinical blood samples contain some species with oxygenated or deoxygenated form, which can also bring signal interference in the visible region. Roggan et al. demonstrated that the absorption minimum of fully deoxygenated whole blood was at 805 nm and maxima were at 420 and 540 nm.[18,19] Near-infrared quantum dots (NIR QDs) can improve the penetrative ability of light at this wavelength through whole blood and minimize tissue autofluorescence. Recently, Stewart et al. used NIR QDs ECL to detect dopamine in whole blood without the need for any pretreatment or extraction. The two works confirmed that ECL emission in the NIR region will suffer significantly less influence from actual blood samples compared to emission in the visible region.[20] Therefore, developing signal-amplified NIR ratiometric ECL is

Received: May 18, 2016
Accepted: July 20, 2016
Published: July 20, 2016

DOI: 10.1021/acs.analchem.6b01935
Anal. Chem. 2016, 88, 8179−8187

significant for improving the sensitivity and accuracy of complex bioassay.

However, to achieve signal-amplified NIR ratiometric ECL analysis, four major issues should be addressed first: (i) seeking a stable NIR emitter and efficient acceptor of energy transfer; (ii) shortening the distance between the donor and acceptor; (iii) fabricating a dual-role intermediate that integrates the quenching effect and catalytic reaction; (iv) amplifying signals. $CdTe_{core}/CdS_{shell}$ QDs and gold nanorods (AuNRs) can serve as a pair of well-matched donor and acceptor in the near-infrared range, because the extent of spectral overlap between them can be easily tuned by changing the shell thickness of CdS or the aspect ratio of AuNRs.[21−24] However, there is no clear quenching mechanism of AuNRs to QDs whether it follows the Förster resonance energy transfer (FRET) model or nanometal surface energy transfer (NSET) model, because aspherical AuNRs break down the point-dipole approximation at a distance and the uncertain relative orientation of AuNRs influences the distance dependence of energy transfer.[21] Fortunately, the ascertainable correlation between the quenching efficiency of NIR QDs and the number of AuNRs at a fixed separation distance provides an effective strategy to quantitatively determine protein or DNA. In addition, graphene oxide (GO) also can serve as a long-range superquencher to most fluorophores (including fluorescent dye, chemiluminescence reagents, QDs, etc.) because of the nonradiative electronic transference from fluorophore excited states to the π-system of GO.[25] Therefore, AuNRs/GO nanocomposites can bring about a dual/synergetic quenching to NIR QDs. Besides, to shorten the distance between the donor and acceptor, a series of binding modes have been developed, such as electrostatic assembly,[26] $\pi-\pi$ stacking interaction,[27] supramolecular recognition,[28] DNA hybridization,[29] and special recognition (antigen−antibody,[30] protein−aptamer,[31,32] avidin−biotin,[33] mannose−lectin[34]). Protein−aptamer recognition has attracted great research interest in energy transfer sensing, because many aptamers can form stable and folded three-dimensional (3D) G-quadruplex (G_4) structure after binding to protein. Moreover, the G_4 structure can load the hemin (iron protoporphyrin, the active center of heme proteins) to form G_4H DNAzyme which has high peroxidase-like activity without some disadvantages of the natural enzymes (such as instability, long-time consumption, and high-cost purification process).[35] On the basis of these findings in previous studies, if GO, hemin, AuNRs, and G_4H DNAzyme can be integrated together, signal-amplified NIR ratiometric ECL sensors may be easily obtained.

Herein, we prepared an rGO−H−AuNRs−G_4H composite and used it as both quencher and enhancer to fabricate an ultrasensitive and self-calibrated NIR ratiometric ECL aptasensor (Scheme 1). The rGO−H composite obtained by $\pi-\pi$ stacking interaction of hemin and rGO could serve as an excellent platform for in-site growth of AuNRs. After the thrombin aptamer (TBA_2) was connected with rGO−H−AuNRs ternary nanocomposite, the rGO−H−AuNRs−G_4H composite would be formed via the induction of hemin or specific recognition of TB. Dual-quenching effect and multiple enhancement effects could be achieved by the nanocomposite. On one hand, the dual quenching was derived from AuNRs, rGO−H, and 3D G_4 structure, because as acceptors both AuNRs and rGO−H showed a high extent of spectral overlap with NIR-emitting QDs and the folded 3D G_4 structure greatly shortened the distance between rGO−H−AuNRs and NIR QDs. Thus, a dual electrochemiluminescence energy transfer

Scheme 1. (A) Schematic Illustration of ECL Aptasensor for Detection of Thrombin, and (B) Fabrication Procedures of rGO−H−AuNRs−G_4H

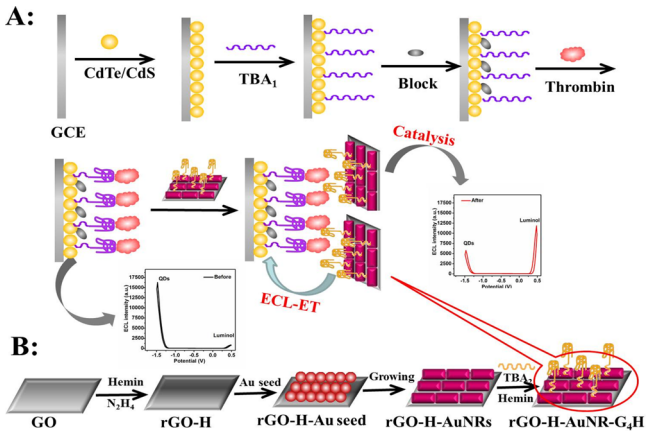

(ECL-ET) between NIR QDs and rGO−H−AuNRs−G_4H resulted in a dramatic reduction of ECL intensity of NIR QDs. On the other hand, the multiple enhancement effects of the ECL of luminol were attributable to AuNRs and dual hemin intercalated into G_4 structure and connected onto rGO. Therefore, the rGO−H−AuNRs−G_4H composite could achieve multiple peroxidase-like catalysis of H_2O_2 to greatly enhance the ECL of luminol. Furthermore, it was successfully used for fabricating a ratiometric NIR ECL immunosensor through a "TBA_1−TB−TBA_2" sandwich mode, which demonstrated excellent ECL immunoassay performance.

EXPERIMENTAL SECTION

Reagents. Thrombin aptamers 5′-NH_2−$(CH_2)_6$−GGTTGGTGTGGTTGG-3′ (TBA I) and 5′-SH−$(CH_2)_6$−AGTCCGTGGTAGGGCAGGTTGGGGTGACT-3′ (TBA II), IgG (1 mg mL^{-1}), streptavidin (SA), and ATP were purchased from Sangon Biotech Co. Ltd. (Shanghai, China). Graphene oxide (GO) was purchased from Nanjing XFNANO Materials Tech Co., Ltd.

$CdCl_2·2.5H_2O$ (99.0%), $NaBH_4$ (96.0%), tellurium powder (99.9%), bovine serum albumin (BSA), ascorbic acid, tetrachloroauric(III) acid hydrate ($HAuCl_4·4H_2O$, AR), hydrazine monohydrate (85%, AR), H_2O_2 (30%), $NH_3·H_2O$ (GR), and Tween-20 were obtained from Sinopharm Chemical Regent Co. Ltd. (Shanghai, China). Mercaptopropionic acid (MPA, 99%), hemin, thrombin (TB), hexadecyltrimethylammonium bromide (CTAB, 99%), sodium dodecyl sulfate (SDS, 99%), tris(2-carboxyethyl) phosphine (TCEP), *N*-hydroxysuccinimide (NHS), and 1-ethyl-3-(3-(dimethylamino)propyl) carbodiimide hydrochloride (EDC·HCl) were obtained from Sigma-Aldrich Chemicals Co. (Shanghai, China).

All other common solvents and salts were of analytical grade and were used as received. Phosphate-buffered saline (PBS) was prepared by mixing PB solution with 0.9% NaCl. Ultrapure water (Mill-Q, Millipore, 18.2 MΩ cm resistivity) was used throughout the experiments.

Apparatus. The ECL emission was recorded using a model MPI-EII ECL analyzer (Xi'an Remex Electronic Science and Technology Co. Ltd., China). All ECL experiments were performed in a 10 mL glass cell with a conventional three-electrode system composed of Ag/AgCl (saturated KCl) electrode as the reference electrode, a platinum wire as the

DOI: 10.1021/acs.analchem.6b01935
Anal. Chem. 2016, 88, 8179−8187

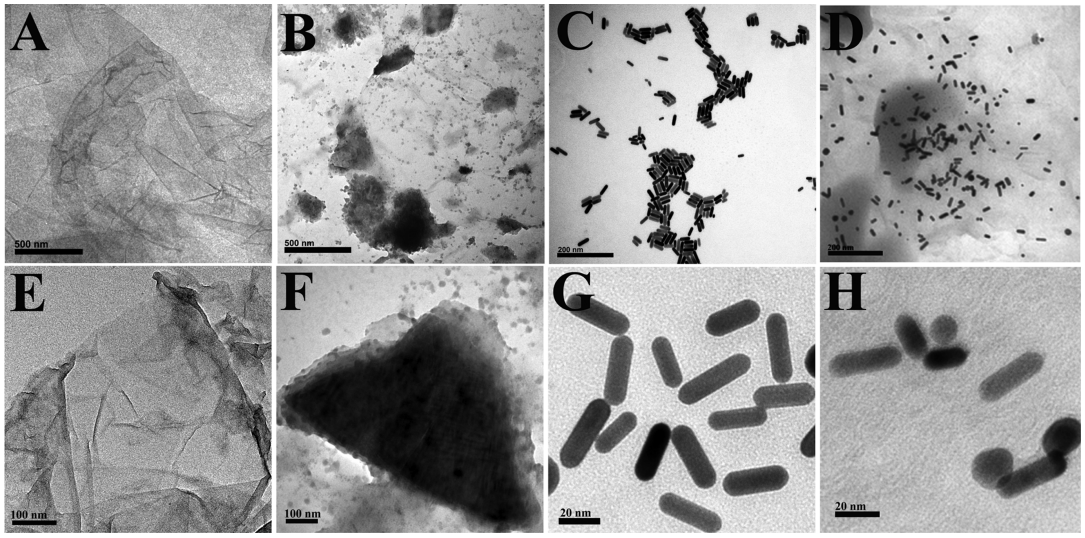

Figure 1. TEM images with different magnifications of (A and E) rGO, (B and F) rGO−H, (C and G) AuNRs, and (D and H) rGO−H-AuNRs.

auxiliary electrode, and bare or modified glass carbon electrodes (GCE, 3 mm diameter) as the working electrodes.

Cyclic voltammetry (CV) and electrochemical impedance spectroscopy (EIS) analyses were performed with a CHI 660E electrochemical workstation (CH Instrument Co. Shanghai) in the solution of 0.5 M KCl containing 5 mM $K_3[Fe(CN)_6]$/$K_4[Fe(CN)_6]$, using the same three-electrode system in the ECL detection.

Ultraviolet−visible (UV−vis) absorption spectra were recorded on a Nicolet Evolution 300 UV−vis spectrometer coupled with a 1.00 cm quartz cell (Thermo Nicolet, US). Fourier-transform infrared (FT-IR) spectra were collected on a Nicolet Avatar-330 spectrometer with 4 cm^{-1} resolution using the KBr pellet technique. Raman spectra were recorded with an inVia Raman spectrometer (Renishaw, U.K.) equipped with a He−Ne laser excitation source operating at 633 nm. Photoluminescence (PL) spectra were measured on an Edinburgh FLS920 spectrometer with an integrating-sphere attachment under excitation of 450 nm light. Transmission electron microscopy (TEM) images were acquired using a FEI Tecnai G20 transmission electron microscope operating at an acceleration voltage of 200 kV. X-ray photoelectron spectroscopy (XPS) was measured by a Thermo VG Multilab 2000 spectrometer equipped with a monochromatic Al Kα radiation source at room temperature.

Preparation of rGO−H, rGO−H−AuNRs. The rGO−H was synthesized according to the previous report.[36] Briefly, 20 mg of graphene oxide was mixed with 40 mL of the ultrapure water to form a homogeneous dispersion (0.5 mg/mL) under ultrasonication for 2 h. Then, 40 mL of 0.5 mg/mL hemin aqueous solution was mixed with graphene oxide dispersion under stirring for 15 min, followed by the successive addition of 400 μL of ammonia solution and 60 μL of hydrazine solution. After being vigorously shaken or stirred for a few minutes, the vial was put in a water bath at 60 °C for 3.5 h. The dispersion was filtered and washed several times to obtain rGO−H that could be redispersed readily in water by ultrasonication.

The rGO−H−AuNRs was synthesized on the basis of the recent report with some modifications.[37] Similarly to typical synthesis of AuNRs, the seed solution was prepared by rapidly injecting 0.6 mL of freshly prepared ice-cold $NaBH_4$ solution (0.01 M) into the Au (III)−CTAB mixture containing 0.25 mL of $HAuCl_4$ (0.01 M) and 9.75 mL of CTAB (0.1 M) under gentle stirring for 2−5 min. The solution color changed from yellow to brownish-yellow, and then the solution was stored at 30 °C for 2 h before use. A growth solution was prepared by mixing 50 mL of CTAB (0.1 M), 10 mL of rGO−H dispersion (0.25 mg/mL), 2.5 mL of $HAuCl_4$ (0.01 M), 375 μL of $AgNO_3$ (0.01 M), and 1 mL of HCl (1 M) under gentle stirring at for 5 min, followed by slow addition of about 0.4 mL ascorbic acid (0.1 M) to the mixture. Finally, the growth solution was supplemented with 120 μL of the seed solution and kept undisturbed overnight at 30 °C. The reaction products were isolated by centrifugation at 9000 rpm for 20 min followed by the removal of the supernatant. The precipitates were redispersed in water.

Preparation of rGO−H−AuNRs−G_4H Composite. The rGO−H−AuNRs−G_4H was prepared by Au−S covalent bonding between rGO−H−AuNRs and thiol-modified thrombin aptamer (SH−TBA_2).[38,39] First, 2 mL of rGO−H−AuNRs dispersion was centrifuged at 9000 rpm for 20 min to remove the excess CTAB, and then was redispersed in 50 mM Tris−HCl (pH 7.4) buffer solution containing 2% SDS. Subsequently, 200 μLof SH−TBA (1 μM) with deprotection of 0.1 mM TCEP for over 1 h (molar ratio TCEP/SH−TBA = 100:1) was added into the nanocomposite solution, which was then incubated for 16 h and aged for another 12 h with 0.2 M NaCl. Finally, rGO−H−AuNRs−TBA was purified by centrifugation at 10 000 rpm for 5 min and redispersed in water. Then, 100 μL of hemin (2 mg/mL) solution was added under stirring for 2 h to form the rGO−H−AuNRs−G_4H structure. After blocking of the possible remaining active sites with hexanethiol and BSA, the resulting dispersion was then centrifuged at 10 000 rpm and dispersed in 2 mL of Tris−HCl buffer solution (pH 7.4) for further use.

Fabrication of the TBA_1−TB−TBA_2 Sandwich Aptasensor. Scheme 1A displays the preparation of the ratiometric ECL aptasensor. First, CdTe/CdS $core_{small}$/$shell_{thick}$ QDs were prepared according to our previous work (Figure S1).[40] An amount of 5 μL of purified CdTe/CdS QDs solution was drop-cast on the pretreated GCE (GCE, 3 mm diameter) and then air-dried at room temperature for over 4 h to get GCE modified by the CdTe/CdS film. After that, 10 μL of aqueous solution containing EDC (10 mg/mL) and NHS (20 mg/mL) was

DOI: 10.1021/acs.analchem.6b01935
Anal. Chem. 2016, 88, 8179−8187

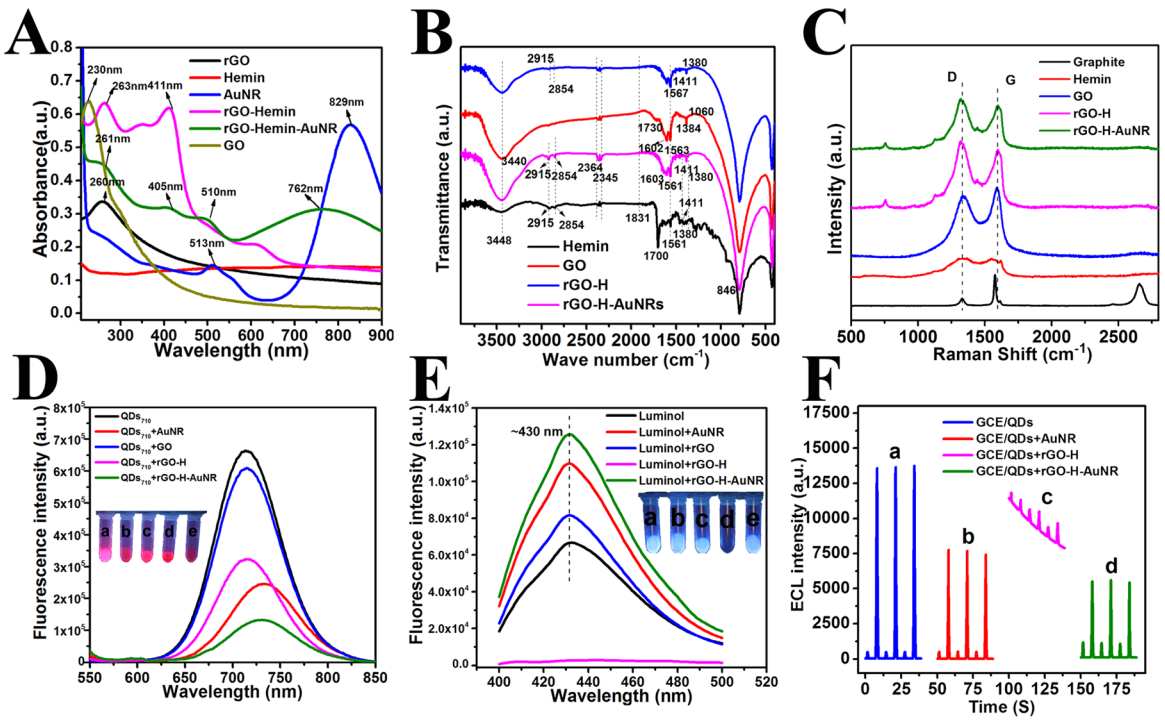

Figure 2. (A) UV−vis absorption spectra of rGO, hemin, AuNR, rGO−H, rGO−H−AuNR, and GO. (B) Infrared spectra of hemin, GO, rGO−H, and rGO−H−AuNR. (C) Raman spectra of graphite, hemin, GO, rGO−H, and rGO−H−AuNR. Fluorescence spectra of (D) QDs and (E) luminol after identical addition of AuNR, rGO, rGO−H, and rGO−H−AuNR. (F) ECL responses of QDs/GCE in different luminol PBS buffers containing water (a), AuNRs (b), rGO−H (c), and rGO−H−AuNRs (d), respectively.

pipetted onto the QDs/GCE surface and incubated for 1 h at 37 °C to activate their COOH groups, and then the GCE was rinsed with PBST to remove excess reactants. Subsequently, 10 μL of amino-modified TBA_1 was drop-cast on the pretreated GCE and then the GCE was covered with a pipet tip for over 12 h at 4 °C under a moist atmosphere. After the residual active sites were thoroughly washed and blocked, the prepared TBA_1/QDs/GCE was incubated in 60 μL of TB suspension for 60 min at 37 °C and then washed with PBST. Finally, the TB/TBA_1/QDs/GCE was incubated in 60 μL of rGO−H−AuNRs−G_4H dispersion (TBA_2) for 60 min at 37 °C, and then washed thoroughly with PBST to remove nonspecifically bounded conjugates for the subsequent ECL characterization assays. Finally, the modified electrode was characterized via ECL measurement in a 0.1 M PB solution (pH 7.4) with 1 mM H_2O_2 using the aforementioned three-electrode system. The ECL measurements were performed from 0.5 to −1.5 V at a scan rate of 300 mV s^{-1}.

RESULTS AND DISCUSSION

Characterization of the Ternary rGO−H−AuNRs Nanocomposite. Scheme 1A displays the preparation process of the four-in-one rGO−H−AuNRs−G_4H composite, which contains three successive steps: the $\pi-\pi$ stacking interaction between hemin and graphene oxide, in-site growth of AuNRs, and surface ligand exchange. As shown in Figure 1, parts A and E, the graphene oxide showed the wrinkled and folded thin-layer morphology. After $\pi-\pi$ stacking interaction between hemin and graphene oxide and subsequent hydrothermal reduction process, rGO−H nanocomposite could be obtained. As can be seen from Figure 1, parts B and F, some aggregated hemin particles are clearly observed on the surface of rGO, indicating the successful assembling of rGO−H nanocomposite. Through the two-step reduction of $HAuCl_4$ by $NaBH_4$ and ascorbic acid, rGO−H−AuNRs could be prepared using in-site seed-mediated growth strategy (Figure 1, parts D and H). AuNRs were uniformly dispersed on the surface of rGO−H with some inevitable spherical gold nanoparticles (Figure 1, parts C and G), indicating that the wrinkled and folded rGO−H platform prevents the aggregation of AuNRs but may hinder the growth of AuNRs at the same time. The average size of the modified AuNRs is estimated to be 30 mm × 10 nm.

The UV−vis absorption spectrum was used for indirectly investigating the preparation process of these nanocomposites. As can be seen in Figure 2A, the GO dispersion showed a strong absorption at 231 nm, which is due to the $\pi \rightarrow \pi^*$ transition of aromatic C═C bonds, and a shoulder peak at about 290−300 nm, which corresponds to the n−π^* transition of the C═O bond.[41] As control, the rGO under the reduction of hydrazine hydrate presents a strong absorption at 261 nm due to the $\pi \rightarrow \pi^*$ transition of the aromatic C═C bond, indicating the restoration of the π-conjugation network. Hemin displayed a weak peak at 385 nm ascribed to the Soret band, as well as a group of weak peaks between 500 and 700 nm attributed to the Q-bands. The rGO−hemin (rGO−H) exhibited two strong absorption peaks at 263 and 411 nm, which, respectively, correspond to the characteristic absorption peak of rGO and the Soret band of hemin. Notably, the Soret band of hemin displayed a large red shift (~26 nm), indicating the $\pi-\pi$ interaction between GO and porphyrin moiety of hemin.[42] All these results clearly demonstrate that hemin molecules were attached to graphene. After the in-site growth of AuNRs on the surface of rGO−H, two strong absorption peaks emerged at approximately 510 and 762 nm, which correspond to the surface plasmon absorption of AuNRs, indicating the successful preparation of rGO−H−AuNRs. The

DOI: 10.1021/acs.analchem.6b01935
Anal. Chem. 2016, 88, 8179−8187

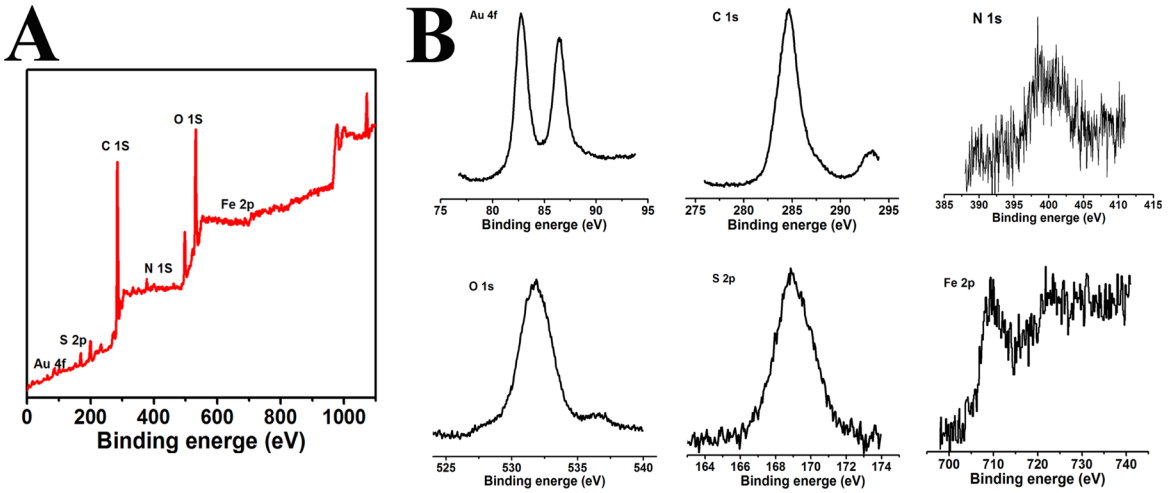

Figure 3. XPS analyses for (A) the full region of XPS for rGO−H−AuNR−TBA_2 bioconjugate and (B) the Au 4f region, C 1s region, N 1s region, O 1s region, S 2p region, and Fe 2p region.

high spectral overlap between QDs and rGO−H−AuNRs would bring about efficient energy transfer (Figure S3).

FT-IR spectra were also used to investigate the formation of rGO−H−AuNRs nanocomposite by distinguishing the infrared absorption characteristic peaks of the functional groups. As shown in Figure 2B, hemin showed an absorption band at 1700 cm^{-1} (corresponding to the C═O stretch mode of carboxylic group), at 1411 cm^{-1} (corresponding to the B_{3u} vibration of porphyrin), and at 846 cm^{-1} (corresponding to ═C−H deformation vibration of olefin).[43] In the spectrum of GO, several characteristic peaks consecutively appeared at 1730, 1602, 1380, and 1060 cm^{-1}, which are, respectively, attributed to the C═O, C═C, C−H, and C−O stretching vibrations. Compared with that of GO, the C═O characteristic absorption of the rGO−H−AuNRs nanocomposites disappeared and the C−O and O−H groups of the rGO−H−AuNRs nanocomposites decreased dramatically, which was caused by the hydrothermal reduction. The C═O stretching vibration of the rGO−H−AuNRs nanocomposites displayed a red shift from 1700 to 1708 cm^{-1} in comparison with that of hemin, which could be attributed to the $\pi-\pi$ aromatic interaction between hemin and rGO.[44] Besides, two identical infrared absorption characteristic peaks were observed at 2915 and 2854 cm^{-1} for hemin, rGO−H, and rGO−H−AuNRs, which also verifies the $\pi-\pi$ stacking between hemin and rGO. These results indicate the effective hydrothermal reduction of GO and successful load of hemin.

Moreover, Raman spectroscopy can be used to verify the formation of rGO−H−Au nanocomposite by examining the ordered/disordered crystal structures (Figure 2C). The characteristic bands of carbons are located at around 1580 and 1350 cm^{-1}, which correspond to the graphite bands (G band, first-order scattering of E_{2g} phonons by sp^2 carbon atoms) and diamondoid bands (D band, breathing mode of κ-point photons of A_{1g} symmetry), respectively.[45] Hemin displays three major bands located at about 1632, 1580, and 1368 cm^{-1}, which are related to the asymmetric C−C stretching and the symmetric pyrrole-half-ring stretching of the protoporphyrin (IX) ring system, respectively.[46] The I_D/I_G of the graphite, GO, and rGO−H increased continuously, implying that graphene sheets changed to be more amorphous and defective upon exfoliation of graphite flakes and the number of graphitic domains became smaller upon reduction. In addition, the similar characteristic bands and the clear increase of I_D/I_G in rGO−H−AuNRs compared with in pure hemin demonstrated the successful attachment of hemin molecules onto rGO.

Figure 2, parts D and E, respectively, show the fluorescence changes of QDs and luminol after the addition of equal amounts of AuNRs, rGO, rGO−H, and rGO−H−AuNRs dispersion. In terms of QDs, the fluorescence quenching rates of the above materials are 62.9%, 8.2%, 51.3%, and 80.0%, implying that the rGO, hemin, and AuNRs can synergistically quench QDs and there is no mutual inhibition among them. As for luminol−H_2O_2, AuNRs, rGO, and rGO−H−AuNRs could promote the fluorescence while rGO−H showed annihilation effect to luminol, which may be caused by the excessive hemin. After growth of AuNRs on rGO−H, the blocking effect of AuNRs and the loss of hemin might reduce the annihilation of luminol. In addition, for directly verifying the ECL synergistic effect, the QDs were dispensed onto GCE and tested in different PBS buffers containing luminol, luminol plus AuNRs, luminol plus rGO−H−AuNRs, and luminol plus rGO−H−AuNRs−TBA_2 plus hemin, respectively. ECL signal changes of QDs and luminol are shown in Figure 2F. Curve a shows stable dual ECL signals from QDs and luminol as the control experiment. AuNRs exhibited good ECL quenching ability for QDs but weak ECL enhancement for luminol. Besides, the intensity ratio of $ECL_{luminol}/ECL_{QDs}$ was improved (curve b). A gradually reduced ECL signal and a high background signal can be observed in curve c compared with in curve a, which may result from the presence of hemin. Interestingly, the background signal disappeared and the ECL intensity ratio was improved clearly after the growth of AuNRs on the rGO−H platform. The prominent ECL synergistic effect of the rGO−H−AuNRs−TBA_2−G_4H demonstrates that it can act as a sensitive probe for signal-amplified ratiometric ECL aptasensor.

Characterization of the rGO−H−AuNRs−TBA_2 Bioconjugates. XPS characterization was employed to estimate the chemical composition of rGO−H−AuNRs−TBA_2 bioconjugates (Figure 3). The fully scanned spectra confirmed the existence of gold, sulfur, carbon, nitrogen, oxygen, and iron elements in SH−TBA_2 bioconjugates (Figure 3A). The peak at 398.4 eV, which was assigned to N 1s, might be derived from the porphyrin unit of hemin, CTAB, or TBA_2 (Figure 3B). The characteristic peaks of S 2P (168.97 eV), Au 4f (82.65 eV), and Fe 2p (709.25 eV) were derived from SH−TBA_2, AuNRs, and

DOI: 10.1021/acs.analchem.6b01935
Anal. Chem. 2016, 88, 8179−8187

hemin, respectively, clearly confirming the successful fabrication of rGO−H−AuNRs−TBA_2.[47]

Characterization of the ECL Aptasensor. The stepwise fabrication of the near-infrared ratiometric ECL aptasensor can be demonstrated by CV and EIS. $[Fe(CN)_6]^{4-}/[Fe(CN)_6]^{3-}$ was chosen as the representative electroactive probe. Figure 4A

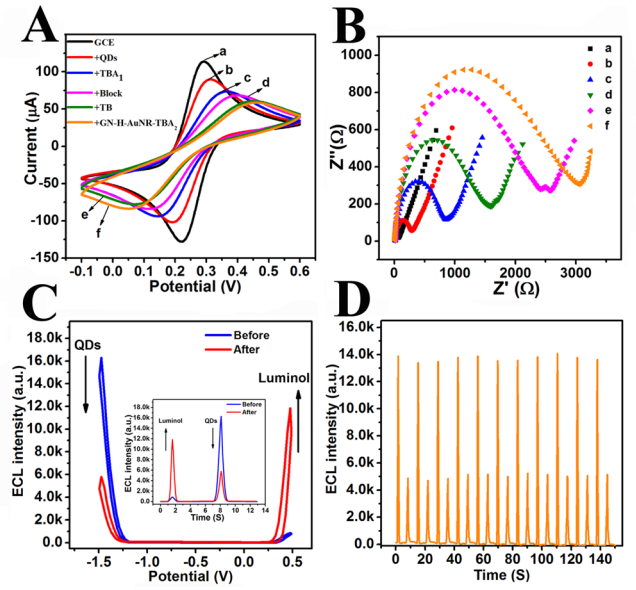

Figure 4. CV (A) and EIS (B) of (a) bare GCE, (b) QDs/GCE, (c) TBA_1/QDs/GCE, (d) block/TBA_1/QDs/GCE, (e) TB/block/TBA_1/QDs/GCE, (f) rGO−H−AuNR−TBA_2/TB/block/TBA_1/QDs/GCE at the TB concentration of 10 pg/mL. (C) ECL responses before and after connecting rGO−H−AuNR−G_4H. (D) ECL signal stability.

shows a pair of symmetric redox peaks (curve a), which correspond to the reversible redox reaction of $Fe(CN)_6]^{3-/4-}$ on the bare GCE. After modification of the QDs, the peak current of the electrode decreased, while the potential difference (ΔE) between oxidation peak and reduction peak increased clearly (curve b), implying that the electrical conductivity of QDs semiconductor is lower. With a further decrease of the peak currents in the CV curves, the gap between the anodic and cathodic peaks became wider in the subsequent stepwise assembly processes of TBA_1, blocking agent, and TB because of the electrostatic repulsion between the negative charges of the TBA_1 phosphate backbone and the Fe-$(CN)_6]^{3-/4-}$ and the electrical inertness of protein. However, the peak current of the electrode slightly increased when connecting G_4H−AuNRs−H−rGO to the electrode by the specific recognition of TB and TBA_2, which was attributed to the excellent electrical conductivity of AuNRs and rGO in the four-in-one composite. These changes obviously indicate the successful fabrication of ECL aptasensor for detection of TB.

Furthermore, the Nyquist plots of EIS spectra can be used to display the changes in the surface features of the modified electrodes in the assembly process (Figure 4B). The diameter of the semicircle in a higher frequency range of the Nyquist plots indicates the electron-transfer resistance (R_{et}) at the electrode interface. The bare GCE exhibited a lower R_{et} than QD/GCE due to the weaker electronic transfer capability of QDs (curves a and b). With the sequential assembly of TBA_1 (curve c), blocking agent (curve d), TB (curve e), and TBA_2 (curve f), the R_{et} increased steadily. The result of EIS was basically consistent with the CV, confirming the successful preparation of the aptasensor.

The sandwich immunoassay was further confirmed by ECL measurements (Figure 4C). A strong cathodic ECL signal (∼−1.5 V) from QDs and a weak anodic ECL signal from luminol (∼+0.45 V) were observed simultaneously. The possible mechanism of the dual-potential ECL ratiometric strategy is shown in Figure S3. Before connection of rGO−H−AuNRs−TBA_2−G_4H probe, the ECL peak of QDs was much higher than that of luminol and the value of $ECL_{luminol}/ECL_{QDs}$ was determined to be about 1:14. After multiple catalytic reactions and dual quenching from rGO−H−AuNRs−TBA_2−G_4H probe, the ECL peak of luminol was higher than that of QDs and the value of $ECL_{luminol}/ECL_{QDs}$ was calculated to be 2:1, indicating successful preparation of the near-infrared ratiometric ECL aptasensor. In addition, Figure 4D shows the signal stability of the ratiometric aptasensor in the process of ECL testing. With ECL testing for 20 cycles from +0.5 to −1.5 V, the ECL signals of QDs and luminol showed synchronous fluctuation within a narrow range, but the intensity ratio ($ECL_{luminol}/ECL_{QDs}$) was relatively constant, indicating high stability of the ratiometric aptasensor.

Signal Amplification of rGO−H−AuNRs−G_4H for ECL Aptasensor. The roles of three amplifying mediums (AuNRs, rGO−H, and G_4H) were confirmed by comparing the signal intensities of the four different aptasensors for detecting TB (1 ng mL^{-1}). Parts A and B of Figure 5 separately show the ECL spectra and detailed ECL intensities of the four aptasensors. The AuNRs showed an enhanced ECL intensity ratio (curve b).

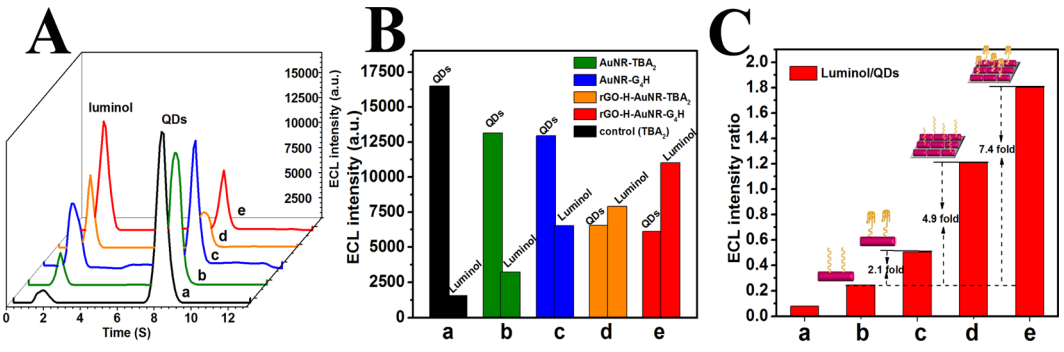

Figure 5. (A) ECL spectra, (B) ECL intensities of QDs and luminol, and (C) $ECL_{luminol}/ECL_{QDs}$ of (a) AuNRs−TBA_2/block/TBA_1/QDs/GCE, (b) AuNRs−G_4H/block/TBA_1/QDs/GCE, (c) rGO−H−AuNRs−TBA_2/block/TBA_1/QDs/GCE, (d) rGO−H−AuNRs−G_4H/block/TBA_1/QDs/GCE.

DOI: 10.1021/acs.analchem.6b01935
Anal. Chem. 2016, 88, 8179−8187

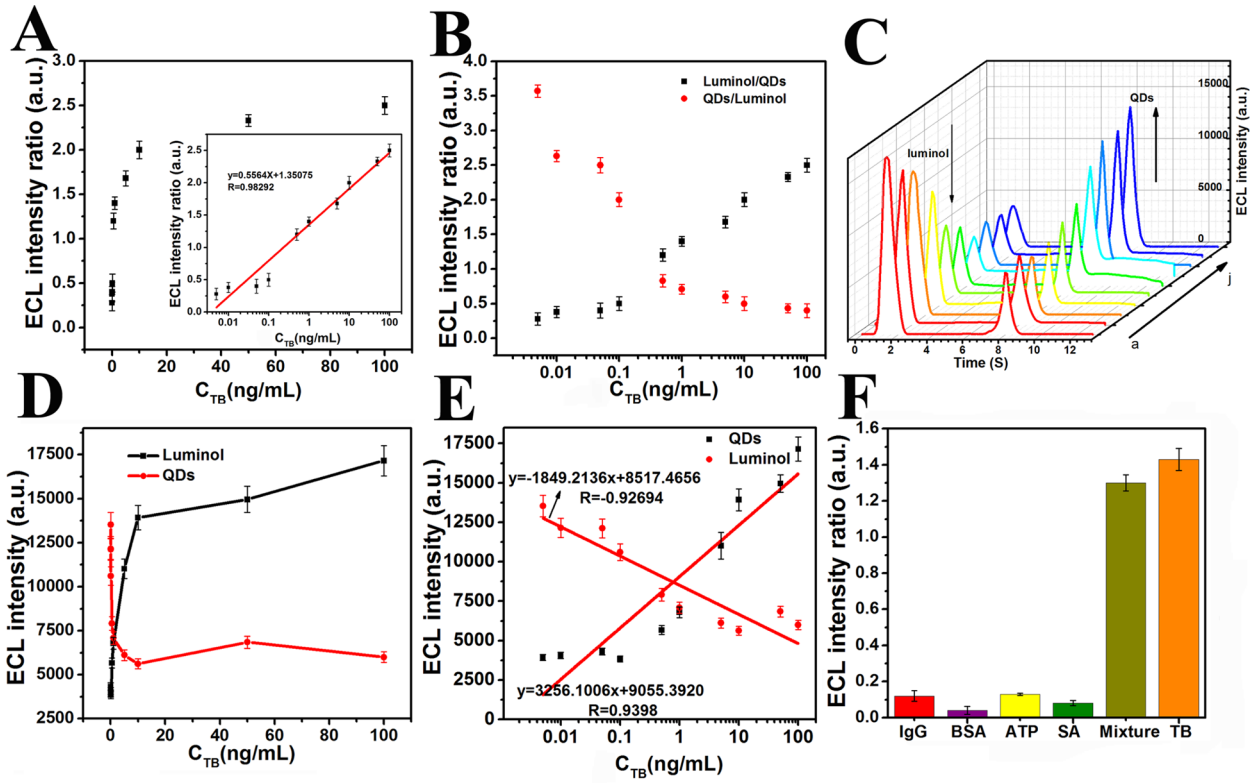

Figure 6. (A) Calibration curve of $ECL_{luminol}/ECL_{QDs}$, (B) dual-signaling ECL intensity ratio of QDs and luminol, (C) ECL profiles, (D) single-signaling ECL intensities of QDs and luminol, and (E) calibration curve of $ECL_{luminol}$ and ECL_{QDs} for determining different concentrations of TB (100 ng/mL to 0.5 pg/mL) in 0.1 M pH 7.4 PB solution containing 2 mM H_2O_2 from 0.5 to −1.5 V at a scan rate of 300 mV s^{-1}. (F) Specificity of IgG, BSA, ATP, SA, mixture, and TB.

Although the ECL quenching rate of QDs was improved and ECL intensity of luminol was increased clearly in curve c compared with curve b, the baseline of curve b fluctuated slightly, which might be caused by the addition of hemin. The high baseline interference was consistent with the results in Figure 2F. In curves d and c, the ECL intensities of QDs were reduced by about 50% and the ECL intensities of luminol were improved by approximately 3−4-fold as compared in curves b and a, respectively, which verifies the signal amplification of rGO−H. Furthermore, when comparing curve c with curve b and curve e with curve d, we found that the ECL intensity of QDs was unimpaired while that of luminol was improved clearly after the formation of 3D G_4H structure. The calculated values of $ECL_{luminol}/ECL_{QDs}$ are shown in Figure 5C. Although pure AuNR can serve as both the quencher and enhancer, the slight enhancement for ECL of luminol indicates its insignificant role in the ratiometric ECL biosensor. After the integration of AuNRs−TBA_2, further integration of rGO−H and G_4H improved the values of $ECL_{luminol}/ECL_{QDs}$ by 4.9-fold and 7.4-fold. These results demonstrate that integrating AuNRs, rGO−H, and G_4H contributes to an excellent synergetic amplification.

ECL Detection of TB. The related influence factors of ECL detection (scanning rate and incubation time of Ab_1) were first investigated. The analytical performance of the approach was characterized under optimal experimental conditions (Figure S5). As shown in Figure 6C, with decreasing TB concentration, the cathodic ECL signal from NIR QDs increased and the anodic ECL signal from luminol decreased simultaneously. The value of $ECL_{luminol}/ECL_{QDs}$ was linearly dependent on the logarithm of TB concentration in the range from 100 ng/mL to 0.5 pg/mL (Figure 6A). The linear regression equation is R_{ECL} (au) = 0.5564 log C_{TB} + 1.35075 with the correlation coefficient R^2 = 0.96613, where R_{ECL} is the ratio of $ECL_{luminol}/ECL_{QDs}$ and C_{TB} is the TB concentration. The limit of detection (LOD) corresponding to a signal-to-noise ratio of 3 was estimated to be 4.2 fg/mL. Figure 6B shows the values of $ECL_{luminol}/ECL_{QDs}$ and $ECL_{QDs}/ECL_{luminol}$, which also confirm the good linear relation between the logarithm of TB concentration and ECL intensity ratio. To prove the superior precision of the dual-signal detection mode, parts D and E of Figure 6 present the ECL single-signal detection results and respective calibration curves of QDs and luminol. The LODs of QDs and luminol corresponding to a signal-to-noise ratio of 3 were estimated to be 1.8 and 2.1 pg/mL, respectively. The higher error and signal fluctuation, unsatisfactory LODs, and lower R value of single-signal detection indicate the superiority of the ratiometric ECL detection mode.

Specificity, Reproducibility, and Stability of the Aptasensor. The specificity of the aptasensor was tested by comparing the ECL responses after the addition of equal amounts of TB, or some other proteins such as IgG, BSA, ATP, streptavidin (SA), or a mixture of them (TB/IgG/BSA/ATP/SA = 0.2:0.2:0.2:0.2:0.2). As shown in Figure 6F, a stronger ECL intensity ratio was obtained from the addition of TB or the mixture, while only very weak intensity ratios emerged after the addition of IgG, BSA, ATP, and SA. Additionally, the two stronger ECL signals resulted from the addition of TB and the mixture were fitted to the linear regression equation. The results demonstrate high specificity of the proposed aptasensor for TB detection. The reproducibility of the aptasensor was investigated with intra- and interassay precision. The intra-assay

DOI: 10.1021/acs.analchem.6b01935
Anal. Chem. 2016, 88, 8179−8187

precision was investigated by assaying the same TB level (1 ng/mL) for five similar measurements. The similar ECL intensities demonstrate that the aptasensor possesses an acceptable reproducibility. Furthermore, the aptasensor was found to retain 89% of the original ECL response after 7 days of storage in 0.01 M PB solution at 4 °C.

Detection of TB in Clinical Serum Samples. For assessing the feasibility of the developed ratiometric ECL aptasensor for TB detection, the practical applicability was investigated by adding different concentrations of TB into normal human serum samples obtained from the Huazhong Agricultural University Hospital (Wuhan, China). Several ECL aptasensors were fabricated by incubation in the diluted normal human serum samples (0.1 M PBS, pH 7.4). The recovery test was performed using the standard addition method. The results are presented in Table 1. The recovery rates of the serum samples ranged from 90.1% to 109.6% and RSDs varied from 2.9% to 5.2%, thereby validating the reliability and practicality of this method.

Table 1. Standard Addition Recovery Experiments of TB

sample	added (pg mL^{-1})	detected (pg mL^{-1})	recovery (%)	RSD (%, n = 3)
1	5	5.18	103.6	2.9
2	10	9.01	90.1	4.6
3	20	18.54	92.7	3.8
4	50	54.80	109.6	5.2

CONCLUSIONS

In this study, a signal-amplified NIR ratiometric ECL detection strategy was developed based on the rGO−H−AuNRs−G_4H composite. This strategy not only broadens the wavelength range of dual-signal ratiometric strategy from visible light to NIR, but also introduces signal amplification into ratiometric ECL sensors, which can meet the demand for high sensitivity and accuracy. Most interference can be eliminated by cross-reference of two emission bands, and the rGO−H−AuNRs−G_4H composite greatly improves the detection sensitivity for TB. Three conclusions could be drawn for the synergetic signal amplification: (i) the high spectral overlap of AuNR and rGO−H with NIR $CdTe_{core}/CdS_{shell}$ QDs contributes to excellent quenching efficiency; (ii) rGO−H with a large surface area and electron transport rate not only provides a good platform for loading more AuNRs but also improves the ECL intensity of luminol; (iii) the secondary hemin intercalated into the folded 3D G_4 structure greatly enhances the signal of luminol. Furthermore, the signal-amplified ratiometric ECL sensing strategy could serve as a universal "mode" for developing other amplified ratiometric ECL sensors by only using different synergetic nanocomposites, which sheds new light on the development of highly sensitive and accurate ratiometric ECL sensors.

ASSOCIATED CONTENT

Supporting Information

The Supporting Information is available free of charge on the ACS Publications website at DOI: 10.1021/acs.analchem.6b01935.

TEM of QDs, photo of colorimetric data, possible mechanism of the dual-potential NIR-ECL ratiometric sensors and CV of the dual-signaling, ECL responses of QDs/GCE in different luminol PBS buffers containing GO and hemin, optimization of incubation time and scanning rate, and comparison of the aptasensors for thrombin (PDF)

AUTHOR INFORMATION

Corresponding Author

*E-mail: hyhan@mail.hzau.edu.cn. Phone: +86-27-87288505. Fax: +86-27-87288505.

Notes

The authors declare no competing financial interest.

ACKNOWLEDGMENTS

We gratefully acknowledge the financial support from National Natural Science Foundation of China (21375043, 21175051).

REFERENCES

(1) Deng, S.; Lei, J.; Cheng, L.; Zhang, Y.; Ju, H. *Biosens. Bioelectron.* **2011**, *26*, 4552−4558.
(2) Jie, G.; Li, L.; Chen, C.; Xuan, J.; Zhu, J. J. *Biosens. Bioelectron.* **2009**, *24*, 3352−3358.
(3) O'Reilly, E. J.; Keyes, T. E.; Forster, R. J.; Dennany, L. *Analyst* **2013**, *138*, 677−682.
(4) Bertoncello, P.; Stewart, A. J.; Dennany, L. *Anal. Bioanal. Chem.* **2014**, *406*, 5573−5587.
(5) Zanarini, S.; Rampazzo, E.; Ciana, L. D.; Marcaccio, M.; Marzocchi, E.; Montalti, M.; Paolucci, F.; Prodi, L. *J. Am. Chem. Soc.* **2009**, *131*, 2260−2267.
(6) Zhou, X. M.; Xing, D. B.; Zhu, D.; Jia, L. *Anal. Chem.* **2009**, *81*, 255−261.
(7) Xu, S.; Liu, Y.; Wang, T.; Li, J. *Anal. Chem.* **2011**, *83*, 3817−3823.
(8) Xu, W.; Yi, H.; Yuan, Y.; Jing, P.; Chai, Y.; Yuan, R.; Wilson, G. S. *Biosens. Bioelectron.* **2015**, *64*, 423−428.
(9) Shao, K.; Wang, J.; Jiang, X.; Shao, F.; Li, T.; Ye, S.; Chen, L.; Han, H. *Anal. Chem.* **2014**, *86*, 5749−5757.
(10) Zhang, P.; Wu, X.; Yuan, R.; Chai, Y. *Anal. Chem.* **2015**, *87*, 3202−3207.
(11) Mohsan, Z.; Kanibolotsky, A. L.; Stewart, A. L.; Inigo, A. R.; Dennany, L.; Skabara, P. J. *J. Mater. Chem. C* **2015**, *3*, 1166−1171.
(12) Zhang, H. R.; Xu, J. J.; Chen, H. Y. *Anal. Chem.* **2013**, *85*, 5321−5325.
(13) Cheng, Y.; Huang, Y.; Lei, J.; Zhang, L.; Ju, H. *Anal. Chem.* **2014**, *86*, 5158−5163.
(14) Zhao, H. F.; Liang, R. P.; Wang, J. W.; Qiu, J. D. *Chem. Commun.* **2015**, *51*, 12669−12672.
(15) Feng, Q. M.; Shen, Y. Z.; Li, M. X.; Zhang, Z. L.; Zhao, W.; Xu, J. J.; Chen, H. Y. *Anal. Chem.* **2016**, *88*, 937−944.
(16) Hao, N.; Li, X. L.; Zhang, H. R.; Xu, J. J.; Chen, H. Y. *Chem. Commun.* **2014**, *50*, 14828−14830.
(17) Zhang, H. R.; Wu, M. S.; Xu, J. J.; Chen, H. Y. *Anal. Chem.* **2014**, *86*, 3834−3840.
(18) Roggan, A.; Friebel, M.; Doerschel, K.; Hahn, A.; Müller, G. *J. Biomed. Opt.* **1999**, *4*, 36−46.
(19) Dennany, L.; Innis, P. C.; Wallace, C. G.; Forster, R. J. *J. Phys. Chem. B* **2008**, *112*, 12907−12912.
(20) Stewart, A. L.; Hendry, J.; Dennany, L. *Anal. Chem.* **2015**, *87*, 11847−11853.
(21) Li, L.; Chen, Y.; Lu, Q.; Ji, J.; Shen, Y.; Xu, M.; Fei, R.; Yang, G.; Zhang, K.; Zhang, J.-R.; Zhu, J.-J. *Sci. Rep.* **2013**, *3*, 1529.
(22) Gao, J. X.; Bender, C. M.; Murphy, C. J. *Langmuir* **2003**, *19*, 9065−9070.
(23) Gole, A.; Murphy, C. J. *Chem. Mater.* **2004**, *16*, 3633−3640.
(24) Bao, H. B.; Gong, Y. J.; Li, Z.; Gao, M. Y. *Chem. Mater.* **2004**, *16*, 3853−3859.
(25) Bi, S.; Zhao, T.; Luo, B. *Chem. Commun.* **2012**, *48*, 106−108.

DOI: 10.1021/acs.analchem.6b01935
Anal. Chem. 2016, 88, 8179−8187

(26) Kostiainen, M. A.; Hiekkataipale, P.; Laiho, A.; Lemieux, V.; Seitsonen, J.; Ruokolainen, J.; Ceci, P. *Nat. Nanotechnol.* **2012**, *8*, 52−56.
(27) Janiak, C. *J. Am. Chem. Soc. Dalton* **2000**, 3885−3896.
(28) He, L.; Yang, X.; Zhao, F.; Wang, K.; Wang, Q.; Liu, J.; Huang, J.; Li, W.; Yang, M. *Anal. Chem.* **2015**, *87*, 2459−2465.
(29) Shan, Y.; Xu, J. J.; Chen, H. Y. *Chem. Commun.* **2009**, 905−907.
(30) Houghten, A. R. *Proc. Natl. Acad. Sci. U. S. A.* **1985**, *82*, 5131−5135.
(31) Tang, Z. W.; Mallikaratchy, P.; Yang, R. H.; Kim, Y.; Zhu, Z.; Wang, H.; Tan, W. H. *J. Am. Chem. Soc.* **2008**, *130*, 11268−11269.
(32) Zayats, M.; Huang, Y.; Gill, R.; Ma, C. A.; Willner, I. *J. Am. Chem. Soc.* **2006**, *128*, 13666−13667.
(33) Huang, H.; Tan, Y.; Shi, J.; Liang, G.; Zhu, J. J. *Nanoscale* **2010**, *2*, 606−612.
(34) Debruyne, E. N.; Delanghe, J. R. *Clin. Chim. Acta* **2008**, *395*, 19−26.
(35) Lin, D.; Wu, J.; Wang, M.; Yan, F.; Ju, H. *Anal. Chem.* **2012**, *84*, 3662−3668.
(36) Guo, Y. J.; Deng, L.; Li, J.; Guo, S. J.; Wang, E. K.; Dong, S. J. *ACS Nano* **2011**, *5*, 1282−1290.
(37) Liu, J.; Xin, X.; Zhou, H.; Zhang, S. *Chem. - Eur. J.* **2015**, *21*, 1908−1914.
(38) Wang, J.; You, M.; Zhu, G.; Shukoor, M. I.; Chen, Z.; Zhao, Z.; Altman, M. B.; Yuan, Q.; Zhu, Z.; Chen, Y.; Huang, C. Z.; Tan, W. *Small* **2013**, *9*, 3678−3684.
(39) Shi, D.; Song, C.; Jiang, Q.; Wang, Z. G.; Ding, B. *Chem. Commun.* **2013**, *49*, 2533−2535.
(40) Wang, J.; Han, H.; Jiang, X.; Huang, L.; Chen, L.; Li, N. *Anal. Chem.* **2012**, *84*, 4893−4899.
(41) Li, D.; Müller, M. B.; Gilje, S.; Kaner, R. B.; Wallace, G. G. *Nat. Nanotechnol.* **2008**, *3*, 101−105.
(42) Xu, Y. X.; Zhao, L.; Bai, H.; Hong, W. J.; Li, C.; Shi, G. Q. *J. Am. Chem. Soc.* **2009**, *131*, 13490−13497.
(43) Tu, W.; Lei, J.; Ding, L.; Ju, H. *Chem. Commun.* **2009**, 4227−4229.
(44) Gu, C. J.; Kong, F. Y.; Chen, Z. D.; Fan, D. H.; Fang, H. L.; Wang, W. *Biosens. Bioelectron.* **2016**, *78*, 300−307.
(45) Fan, Z. J.; Kai, W.; Yan, J.; Wei, T.; Zhi, L. J.; Feng, J.; Ren, Y. M.; Song, L. P.; Wei, F. *ACS Nano* **2011**, *5*, 191−198.
(46) Spiro, T. G.; Strekas, T. C. *J. Am. Chem. Soc.* **1974**, *96*, 338−345.
(47) Yang, Z. H.; Zhuo, Y.; Yuan, R.; Chai, Y. Q. *ACS Appl. Mater. Interfaces* **2015**, *7*, 10308−10315.

DOI: 10.1021/acs.analchem.6b01935
Anal. Chem. 2016, 88, 8179−8187